DISCRETE MODELING OF CEMENTITIOUS MATERIALS: FAILURE SURFACES IN PLANE STRESS/STRAIN

V. Balopoulos[1], N. Archontas[2,3] and S. J. Pantazopoulou[1,3]

[1]Department of Civil Engineering
Democritus University of Thrace, Xanthi, GR-67100, Greece
e-mail: vbalop@civil.duth.gr

[2]Department of Electrical Engineering
Democritus University of Thrace, Xanthi, GR-67100, Greece
e-mail: narcho@ee.duth.gr, nikosa@ucy.ac.cy

[3]Department of Civil & Environmental Engineering
University of Cyprus, Nicosia, 1 University Ave., P.O. Box 20537, CY-2109, Cyprus
e-mail: pantaz@civil.duth.gr, pantaz@ucy.ac.cy

Keywords: Cementitious materials, dendrites, modeling, strength.

Abstract. *The solid structure of engineered cement-based matrices comprises a continuous network of flaky dendrites emanating from partially hydrated cement grains. In the paper, the microscopic mechanical behavior of cementitious gel is approximated using a discrete model obtained by random generation of the spatial location of cementitious grains in the solid and a random network of dendrites, with statistically random properties. Calibrated to fit the macroscopic physical characteristics of the matrix (density and mean pore size), the model reproduces several known macroscopic behavioral traits of cementitious materials, including the characteristics of the* ***yield and failure surfaces*** *under the states of plane stress/strain. The measured properties of cement-based composites are successfully reproduced, demonstrating that computational simulation of the mechanical behavior of the material under various stress states is possible, using information from few inexpensive laboratory tests. This emerging framework employs a discrete approximation of the material microstructure, thereby departing from the smeared crack, smeared strain continuum mechanics approach with several advantages.*

1 INTRODUCTION

For several years the behavior of concrete materials has been modeled using the established framework of continuum mechanics. This is based on the concepts of infinitesimal stress and strain, and relies on the existence and quantification of values for the Lamé constants (e.g. the modulus of Elasticity and Poisson's ratio) in order to describe the relationship between the stress and strain tensors. However, the image of cementitious materials in the microscope reveals that the assumption of continuity is grossly inaccurate – the solid structure of the material is amorphous comprising gel macromolecules (C-S-H)–i.e., products of cement hydration that entrap various discontinuities and enclosures (e.g. $Ca(OH)_2$crystals and other mineral formations as well as aggregates, [1–2]). The macromolecules form sheets or sticks that emanate folding randomly in space, generating pores of various sizes owing to the void between them, thereby presenting a great internal surface area. Because of this random solid structure these materials are disproportionately weak in tension, exhibiting easy rupture and cracking in directions normal to tensile stress fields, while they present great robustness and strength to compression [3]. For this reason, cementitious materials are incompatible with the constitutive framework of elasticity, be it linear or nonlinear, as it is realized repeatedly in the poor performance of numerical (Finite Element) approximations of the continuum mechanics approach.

In the last years there has been an emerging effort in the area of concrete modeling to depart from continuum mechanics approaches towards a so-called discrete modeling framework which is more appropriate for semi-brittle materials such as soils, built on the so-called particle modeling approaches. Particles are modeled either as randomly sized spheres in contact or as elements of a lattice ([4–7]); force transfer and solid strength occur by interaction of the particles (i.e. spheres) in contact or by bending/axial stretching of the lattice elements. A disadvantage of the particle modeling approach lies in that the sphere interactions occur only under bearing or frictional contact, whereas they cannot transfer tension unless special contact elements are introduced to supply cohesion to the numerical model.

Recently, a third alternative option for discrete modeling, which is particularly targeted towards cementitious materials has been developed by the authors. In this approach reference is made to the actual structure of the gel hydrates which, rather than spheres in contact, better resemble a system of dendrites, that is cementitious hydrates that grow outwards from a partially hydrated cement grain. A simplistic idealization of this material form is given in Fig. 1(a) from [8]. A starting point in this approach is a random generation of cementitious grains (source nodes, SN), which defines the points of growth of cement hydrates (uniform distribution from a statistic point of view); similarly a random generation of target nodes (TN) defines the orientation of the hydration products which extend from the SN to the TN (see for example Fig. 1(b), [9–10]). The total number of dendrite branches that grow outwards from the cementitious grain is a random variable; similarly random variables are the size of the branches and the shape of their cross section, since a range of possibilities from circular to elliptical shapes are randomly selected.

In this manner a study region is defined, termed *the box* having dimensions in the order of a few micrometers, since the basic length measuring variable is the mean hydraulic distance (MHD), δ_o, which is a measure of the mean radius of pores in the gel, the pores being modeled as circular or rectangular slits. The MHD is calculated as twice the ratio of the total evaporable water content held in the gel (which is an estimate of the available void space), divided by the internal surface area of the gel (per unit volume), both quantities being functions of the water to cement ratio, w_o [1–2]. The MHD, which is the order of a few nanometers, is the fundamental length measure in the proposed method. Therefore, the size of the study region as well as the lengths of the branches that represent the hydrates are given all in multiples of MHD. Denser regions are near the cement grain, being represented by stocky dendrites that occur on the grain making a bulky mass. They are part of the force path since they converge to the cement grain which is represented as a nodal point (with degrees of freedom) in the model. The total solid volume comprises the collective volume of all the dendrite branches.

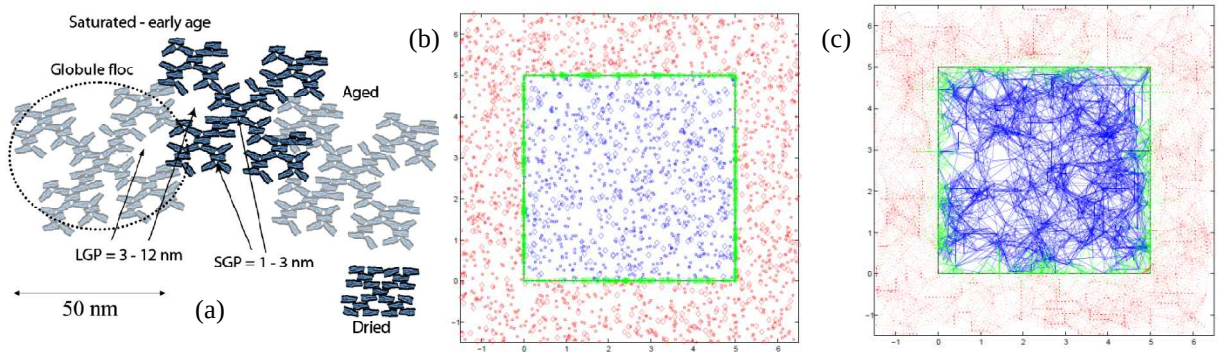

Figure 1. (a) Idealization of packing of cement hydration products (from [8]). (b, c) Definition of mesh for analysis on a discrete 24MHDx24MHD square space and trimming to produce a 15MHDx15MHD central region that is the study *box*. Source nodes (diamonds) and target nodes (circles) are shown in (b) and the branches (lines) generated between them are shown in (c). Blue nodes and solid blue branches lie inside the box. Red nodes and dashed red branches lie outside the box. Green branches lie half inside (solid) and half outside (dashed) the box; new boundary nodes (green) are created for these on the perimeter of the box.

In a previous study a detailed evaluation of the model's performance was carried out based on its ability to reproduce responses that are typical of concrete's behavior under uniaxial tension and compression ([9], [10]). It was found that, with very few input values, the familiar features of concrete's behavior under mechanical load, such as, an almost proportional relationship between stiffness and density, nonlinear stress-strain laws with a softening branch beyond the peak, a compressive strength that is much higher than the uniaxial tensile strength, a consistent value of Poisson's ratio and the dilative behavior with progressive damage are reproduced faithfully by the model. In this stage the model is used to study the behavior of concrete under plane stress – the objective is to estimate, by applying different combinations of boundary conditions in the two principal axes of the coordinate system, the failure envelopes that characterize the material model – again, not by feeding them through a preconceived plasticity or nonlinear elasticity framework, but rather, to obtain them as the output of the model runs under specific boundary constraints. Parameter of study is the ratio of uniaxial strength of the dendrite material in compression (crushing) and tension (fracture). Results are presented in the form of biaxial failure envelopes expressed in the stress and strain space. The validity of the estimations is surmised through comparison with known experimental behavior of cementitious materials under biaxial stress states, such as the familiar biaxial failure envelope of Kupfer and Gerstle[11] shown in Fig. 2 [12], as well as the effect of compression softening due to orthogonal tensile strains and the enhanced deformation capacity of cementitious materials owing to confinement.

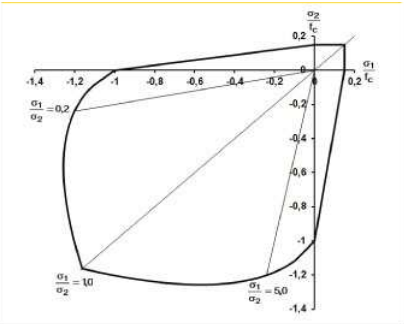

Equation approximating the Kupfer-Gerstle Biaxial Failure envelope in the third quadrant:

$$\left(\beta_1+\beta_2\right)^2-\beta_2-3.65\beta_1=0 \qquad (1)$$

where $\beta_1 = \sigma_1/f_c$ and $\beta_2 = \sigma_2/f_c$, f_c is the concrete uniaxial compressive strength, and $0 > \sigma_1 > \sigma_2$ are the principal stresses (from [12]).

Figure 2: Biaxial Failure Envelope plotted in the stress-space, with principal coordinates being the resultant stress on the box, along the 1 and 2 axes, normalized with respect the uniaxial compressive strength of the material.

2 GENERAL SPECIFICATIONS

2.1 A discrete representation of the cementitious gel

The model studies the box, which is the space trimmed in the core of the region depicted in Fig. 1(c); in the present study, the box is subjected to various states of plane stress by applying displacements or forces along its two principal directions; for reasons of numerical stability, most runs are displacement controlled in both directions, the only exception being unidirectional loading in plane stress. Clearly the model may be extended to 3D, however as is, it already requires great computational effort in order to produce a solution.

To generate the mesh, two uniformly distributed random sets of nodes are generated and superimposed over a square test domain, representing the partially hydrated cement grains (source nodes, SN) and the potential locations of crossing of dendrite branches (target nodes, TN) – the TN being 3 times more dense than the SN. The density of the SN is taken as MHD^{-2} (in 3-D it would be MHD^{-3}), and the MHD is taken equal to 1 μm. In generating branches between SN and TN, not all possible connections are realized. Rather, the probability of realization of any branch is assumed independent of its neighbors and exponential with probability density function $\text{p}(\ell) = \exp\left(-\ell/MHD\right)/MHD$ and cumulative probability function $\text{P}(\ell) = 1-\exp\left(-\ell/MHD\right)$, so as to have the expectation of the cantilevering length ℓ of developing branches equal to MHD. An arbitrary maximum branch length of 3MHD is also enforced.

The node and branch samples are taken over a much wider area than the square element considered in studying the response under uniform loading (referred to hereon as the "box"), in order to ensure that the box is free of boundary artifacts and as representative of "average conditions" as possible. So a typical example case is to generate a study area 24MHD square, which is trimmed to a box of 15MHD square at the center of the study region. For branches that cross the boundary of the box, new nodes lying on the boundary are generated in order to provide an end point for the trimmed branches. Added nodes on the box perimeter are related to two master nodes, so that affine kinematics (macroscopic average conditions) may be enforced locally (as boundary conditions on the box). The first master node (visualized as lying at the origin) is fully fixed and enforces fixity of all negative faces in their respective normal directions. The second master node (visualized as lying at the opposite corner) is used to enforce states of uniform stress and strain. Its last degree of freedom (the y-displacement for 2D, the z- displacement for 3D) is used as the controlling increment in simulation and is always displacement driven, so that softening response may be modeled. On each remaining degree of freedom one may apply displacement or force (either constant or proportional to that of the last degree of freedom). An event to event algorithm is used with constant strain increments $\Delta\varepsilon_2 = \varepsilon_{bf}/200$ along the direction of displacement control. On each occasion, the last converged configuration serves as the starting point for each new increment. The solution uses the standard nonlinear system-solver of Matlab® (Newton with trust region) with default tolerance of 10^{-6} in both displacements and loads.

From past results ([9], [10]) it has been surmised that the cross sectional shape of branches is a critical variable having a marked influence on the results. Best performance was obtained when a random cross sectional shape was assumed for the branches. In the present investigation, the cross section of individual branches may be either circular (*all-rod* networks) or elliptical with random aspect ratio between 1 and 100 (*random-aspect-ratio* networks, closer to physical reality). Note that in loading conditions where extension (direct or transverse) predominates, differences in average response measures between samples of all-rod specimens and samples of random-aspect-ratio specimens are much smaller than differences between specimens within each sample; in fact, they fall below the threshold of statistical significance for unidirectional loading. Such differences, however, become pronounced in compression-dominated loading (i.e., in the third quadrant in stress space of the biaxial failure envelopes). Arithmetic results obtained are consistent with this observation.

Material properties for the dendritic material: branches are idealized as linear elastic elements made of homogeneous and isotropic material of modulus $E_{bf} = \sigma_{bf}/\varepsilon_{bf}$, which rupture in tension at strain ε_{bf} and stress σ_{bf}.

Strain, stress and stiffness are given as multiples of ε_{bf}, σ_{bf}, and E_{bf}, respectively. Branches may fail in compression by crushing or by Euler buckling (followed in both cases by brittle response) – whichever prevails as the controlling mode. For the purposes of force/stiffness state determination and in estimating Euler buckling loads, branches are treated as if they were cylindrical of "average" cross-section. Compressive failure by crushing at strain $10\varepsilon_{bf}$ and stress $10\sigma_{bf}$ is allowed, but rarely occurs in simulation. In this case, which is used as benchmark in the sensitivity study that follows, branch failures in compression are predominantly due to buckling. The calculated biaxial failure envelopes obtained from the model are studied parametrically by considering lower values for the ratios of crushing to tensile strength (specifically 3), revealing that this strength ratio may significantly influence the prevalent mode of dendrite failure in compression with noticeable implications on the form of the failure envelopes.

In the present study, $\varepsilon_{bf} = 10^{-4}$ and $\sigma_{bf} = 10^{+4}$ mN/mm^2 = 10 MPa are used, yielding E_{bf} = 100 GPa, all three values within order of magnitude of measured properties for pure hydrate phases and for cement paste (extrapolated to zero porosity) reported in [1]. Previous studies have illustrated that scale effects can be significant [10]; therefore, only results for boxes of the same dimensions may be quantitatively compared. The average behavior of any sample of boxes of finite dimension is expected to be stiffer and stronger than the material simulated, but it is hard to predict the dependence of simulation results on box dimensions. Several runs of different size boxes would be required to document this sensitivity.

The variability of the numerical results decreases slowly with increasing box size [10], but memory requirements and operation counts increase sharply, following roughly the square and the cube of the box size, respectively. In previous studies by the authors [9–10], specimen dimensions of 24MHD x 24MHD (before trimming) and 15MHD x 15MHD (after trimming, simulated "box") have given results that are reasonably close to macroscopic behavior (in error by roughly 10%, when compared to results for specimens of double the linear dimensions). These specific dimensions were chosen for all specimens in this investigation. About 500MB of RAM is required for each specimen and computation on a small PC of 5 years (available in quantity and at low cost anywhere in the world) takes about one half to one whole day (depending on the range of strains that need be imposed for the chosen type of loading).

2.2 Simulated Response to Static Loading

Results discussed in this work in the following paragraphs concern exclusively 2D specimens, loaded statically under enforced affine kinematics on the boundary for plane-*stress*. Such loading would result in stresses and strains along the axes of the box, if the material was homogeneous and indifferent to orientation; this is indeed the case macroscopically for cement paste, and would be the case asymptotically for boxes of increasing dimensions; thus shear stresses and strains are considered parasitic (an artifact of the small box dimensions) and are ignored. All responses are parameterized by the driving principal strain magnitude and reported as functions of that principal strain value. This is defined as the ratio of the displacement of the last master degree of freedom divided by the length of the specimen side.

Some parameters specific to network generation were chosen a priori and kept constant for all runs, namely the ratio of TN to SN density (set to 3) and the maximum branch length allowed (set to 3MHD). These parameters lead to specimens with material density ~25%. Findings from past studies illustrate that a dominant determining factor of all *stress* and *stiffness* measures of plain cement paste is the *material density*. By contrast, *strain* measures *do not depend* on material density. In the range of values that are relevant to applications, the dependence of stress (and, hence, of stiffness) on material density is almost exactly *linear*. On this finding numerical results obtained from the model are in agreement with experimental evidence. Thus, the effects of specimen density on the results are removed (to within statistical significance) by non-dimensionalization (which involves division of computed stress and stiffness measures by the material density of the specimen).

Results are presented in the form of biaxial failure envelopes of non-dimensionalized stresses and strains (i.e., divided by $\rho\sigma_{bf}$ and ε_{bf}, respectively) that correspond to the first attainment of peak *stress* in either of the principal axes of the coordinate system (i.e., to the limit point beyond which failure would ensue under load control). More data points and larger samples for each point would make for more reliable failure envelopes. Note that the coordinate system, representing either the principal stresses or strains acting on the box sides along x and y (or 1, and 2) defines four quadrants, numbered as follows: Q1 for tension in both axes, Q2 for tension in axis 2 and compression in axis 1, Q3 for compression in both axes, and Q4 for tension in axis 1 and compression in axis 2. Reference to this nomenclature will be made in the forthcoming sections.

3 FAILURE ENVELOPES

3.1 General Framework

The failure envelopes produced in this study differ in the choice of branch cross section (either circular or elliptic with random aspect ratio) and in the presence of nano-reinforcement in the form of multi-wall carbon

nanotubes (either none or targeted at 0.1%, [14–17]). In view of the findings in preceding studies with the proposed model [9–10], differences between failure envelopes are expected to be primarily caused by the difference in branch cross-section and to be more pronounced in the compression-dominated part (Q3).

The introduction of nano-reinforcement is primarily intended for future investigation of its effect on post-limit-point behavior after tension dominated failure (where branch cross-section shape makes little to no difference). Note that based on the experience with the numerical model to this point [9], reinforcing the cementitious material with the addition of MWCNTs in the small amounts commonly used in practice (in the range of ~0.1%) increases the limit stress and strain of the resulting nano-reinforced paste by less than the statistical variability of the results compared [14–17]. Reinforcement of this type seems to significantly increase only the residual load bearing capacity past the limit point, thereby improving the energy absorption of the cementitious structure.

All previous findings are known with certainty only where the global failure mechanism is dominated by cascading failures of branches due to tension in any direction. Conditions near hydrostatic compression require further investigation. In particular, it is necessary to investigate the effect of whether branch failures in compression are predominantly due to buckling or to crushing.

3.2 Primitive data and failure envelopes

Principal results, i.e., the absolutely larger stresses and strains at the limit points, are presented with 2.5 significant digits (2 digits and one rounded to 5 or 0). The same approach is applied to the absolutely smaller stresses and strains at the limit points, but without introducing more decimal digits.

The *location* of limit points (in strain space) is more sensitive than their *value* (in stress space) to the details of post-processing filtering, as should be expected. The particular filtering employed here aims to remove "abrupt" slope changes (signs of numerical divergence) and works well for removing "local" divergences without flattening out the response. A tolerance parameter involved in the algorithm is set at 1.5% in all cases and is only reduced (to 1% or 0.5%) if visual inspection shows that local numerical spikes remain in the vicinity of the limit point of interest.

The C^2 splines, used to produce smooth failure envelopes, are highly sensitive to the details of the values entered. For this reason (i.e., to get better looking failure curves), secondary stress and strain values are rounded independently of primary ones, even though the rounded off values may slightly violate loading constraints (i.e., the ratio of ε_2 to ε_1). Even so, small errors in the data become unwanted artifacts in the C^2 splines, since the "average points" interpolated have statistical variability that may exceed 20%.

Simulation in 2D for compression-dominated loading conditions (Q3 in stress space) should overestimate limit-point stresses and strains, because it implies in-plane compressive failure of many dendrites, whereas out-of-plane tensile failure of dendrites should play a significant role in actual 3D response. Thus, the failure envelopes in the compression dominated zone in stress space are not expected to represent exactly conditions of zero transverse stress (σ_3=0). This effect is particularly pronounced in all-rod networks, where the ensemble of branches is more resistant to compressive failure. In fact, the simulated failure point in 2D equal biaxial compression for all-rod networks with crushing-to-tensile strength ratio set at 10 is so implausible that it is shown in Figure 3 as a black crossed circle, but is not used in interpolations for the failure envelopes.

3.3 Results for high crushing strength (10 times the fracture strength)

These results are grouped in Table 1, for the case of unreinforced paste simulated with branches of circular cross section, and in Table 2, for the case of lightly reinforced paste simulated with branches of random elliptical cross section. The resulting failure envelopes are shown in Figures 3 and 4, respectively. Where branch failures due to direct or indirect extension dominate (pale red part of Tables 1 and 2), the quality of the results is excellent, characterized by low noise (usually filtering with 1.5% tolerance suffices), limited variability (from 5% to 15%), and textbook failure envelopes (see Figures 3 and 4). Furthermore, in tension-dominated response no statistically significant difference is observed between all-rod networks (Table 1 and Figure 3) and random-aspect-ratio networks (Table 2 and Figure 4). The stress failure envelope in Q1, Q2, and Q4 is quite similar to the well known Kupfer-Gerstle envelope [11, 12]. In particular it reproduces the almost constant tensile strength in the Q1 (which is an experimentally established fact) and the nearly linear variation in Q2 and Q4.

In the Q3 of the stress space, simulation results are more noisy (filtering with tolerance 0.5% is often required) and more variable (from 10% to 30%). There is also significant difference (up to 20%) between failure envelopes produced for physically implausible all-rod networks (Figure 3) and more plausible random-aspect-ratio networks (Figure 4), as expected.

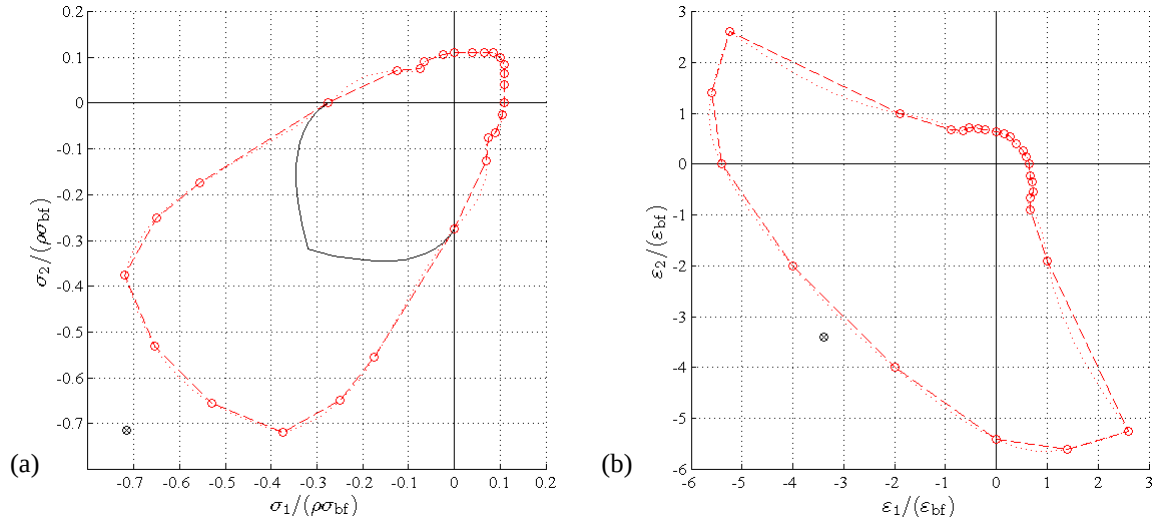

Figure 3: Failure envelopes for 15MHDx15MHD specimens of ***plain*** paste with branches of ***circular*** cross section and of crushing strength ***10 times*** the fracture strength in non-dimensionalized a) stress space and b) strain space. All envelopes are traced by C^0 (dashed) and C^2 (dotted) splines. The Kupfer-Gerstle envelope is plotted as a black solid line. *Note: For $\varepsilon_2=\varepsilon_1 \leftrightarrow \sigma_2=\sigma_1$ in compression, simulated points of maximum stress are shown as crossed circles, but are not used in interpolation.*

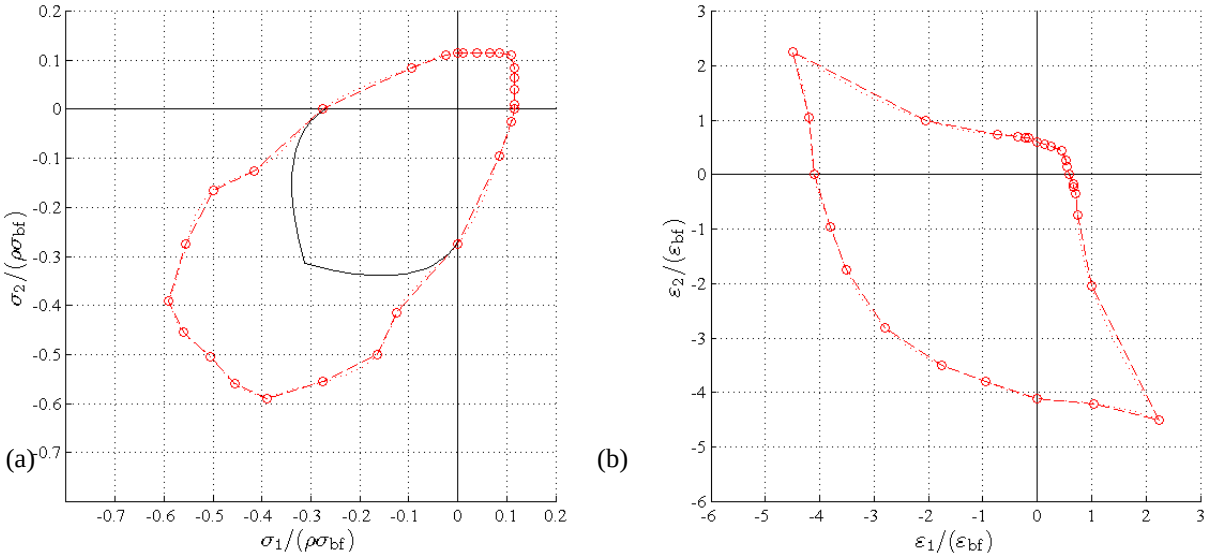

Figure 4: Failure envelopes for 15MHDx15MHD specimens of lightly(~0.1%) ***nano-reinforced*** paste with branches of ***elliptical*** cross section (random aspect ratio) and of ***c***rushing strength ***10 times*** the fracture strength in non-dimensionalized a) stress space and b) strain space. Both envelopes are traced by C^0 (dashed) and C^2 (dotted) splines. The Kupfer-Gerstle envelope is plotted as a black solid line.

Simulated loading under full displacement control for $\varepsilon_2/\varepsilon_1$=–0.5 reproduces almost exactly the point of apparent incompressibility obtained for simulated unidirectional loading (see also [10]), in agreement with experiment [18]. Passage through that point, however, is not followed by immediate failure (as in the case of unidirectional loading), since material disintegration is prohibited by the imposed strain ratio $\varepsilon_2/\varepsilon_1$. For many nearby loading conditions ($\varepsilon_2/\varepsilon_1$ from –0.5 to 0) paths to failure pass near the point ν=0.5 of unidirectional loading, and it is there that a significant number of specimens exhibit global divergence (numerical failure to maintain the imposed $\varepsilon_2/\varepsilon_1$). Furthermore, specimens that avoid divergence exhibit extended plateaus (rather than well localized limit points) and fail at widely disparate strains (anywhere from $3\varepsilon_{bf}$ to above $5\varepsilon_{bf}$). All this is borne out by the failure envelopes in strain space, shown in Figures 3(b) and 4(b), which have each an extensive segment in radial direction and of slope exactly 1/2.

The actual failure envelopes arising from simulation results for high strength against crushing (10 times the strength against fracture), and especially those for random-aspect-ratio networks, are like distorted polygons and are reminiscent of Tresca failure criteria, more pertinent for composite materials. Hence, it is necessary to investigate how the shape and scale of these envelopes are affected by the chosen strength ratio.

Table 1: Non-dimensional stress and strain data for 2D failure envelopes of 15MHDx15MHD ***plain*** paste specimens with branches of ***circular*** cross section and of crushing strength ***10 times*** the fracture strength.

N	n	Loading	$\varepsilon_2/\varepsilon_{bf}$	$\varepsilon_1/\varepsilon_{bf}$	$\sigma_2/(\rho\sigma_{bf})$	$\sigma_1/(\rho\sigma_{bf})$
8	0	$\varepsilon_1=\varepsilon_2$	[+0.400] 15%	[+0.400] 15%	[+0.100] 17%	[+0.100] 17%
8	0	$\varepsilon_1=\varepsilon_2/2$	[+0.535] 9%	[+0.265] 9%	[+0.110] 11%	[+0.085] 11%
8	3	$\varepsilon_1=\varepsilon_2/4$	[+0.595] 6%	[+0.150] 6%	[+0.110] 14%	[+0.065] 13%
5	0	$\varepsilon_1=0$	[+0.620] 7%	0	[+0.110] 7%	[+0.040] 7%
8	0	$\varepsilon_1=-\varepsilon_2/4$	[+0.665] 9%	[–0.165] 9%	[+0.110] 7%	[0.000]
10	1	$\sigma_1=0$	[+0.670] 7%	[–0.225] 9%	[+0.110] 10%	0
14	0	$\varepsilon_1=-\varepsilon_2/2$	[+0.700] 5%	[–0.350] 5%	[+0.105] 15%	[–0.025] 19%
8	2	$\varepsilon_1=-3\varepsilon_2/4$	[+0.720] 8%	[–0.540] 8%	[+0.090] 10%	[–0.065] 17%
10	1	$\varepsilon_1=-\varepsilon_2$	[+0.660] 20%	[–0.660] 20%	[+0.075] 10%	[–0.075] 10%
8	0	$\varepsilon_2=-3\varepsilon_1/4$	[+0.670] 6%	[–0.890] 6%	[+0.070] 13%	[–0.125] 7%
10	1 1	$\sigma_2=0$	[+1.00] 20% [+0.90] 11%	[–1.90] 7% [–1.85] 10%	0	[–0.275] 7% [–0.265] 7%
8 14	1 0	$\varepsilon_2=-\varepsilon_1/2$	[+2.60] 12% [+0.90] 7%	[–5.25] 12% [–1.85] 8%	[–0.175] 22% [0.000]	[–0.555] 17% [–0.265] 8%
8	1	$\varepsilon_2=-\varepsilon_1/4$	[+1.4] 15%	[–5.6] 15%	[–0.25] 25%	[–0.65] 25%
5	1	$\varepsilon_2=0$	0	[–5.40] 6%	[–0.375] 6%	[–0.720] 11%
8	6	$\varepsilon_2=\varepsilon_1/4$	insuff.data	insuff.data	insuff.data	insuff.data
8	3	$\varepsilon_2=\varepsilon_1/2$	[–2.00] 13%	[–4.00] 13%	[–0.530] 12%	[–0.655] 7%
8	4	$\varepsilon_2=\varepsilon_1$	[–3.40] 10%	[–3.40] 10%	[–0.715] 25%	[–0.715] 25%

Table 2: Non-dimensional stress and strain data for 2D failure envelopes of 15MHDx15MHD of lightly (~0.1%) ***nano-reinforced*** paste specimens with branches of ***elliptical*** cross section (random aspect ratio) and of crushing strength ***10 times*** the fracture strength.

N	n	Loading	$\varepsilon_2/\varepsilon_{bf}$	$\varepsilon_1/\varepsilon_{bf}$	$\sigma_2/(\rho\sigma_{bf})$	$\sigma_1/(\rho\sigma_{bf})$
7	0	$\varepsilon_1=\varepsilon_2$	[+0.445] 7%	[+0445] 7%	[+0110] 8%	[+0.110] 8%
8	1	$\varepsilon_1=\varepsilon_2/2$	[+0.525] 9%	[+0.260] 9%	[+0.115] 8%	[+0.085] 9%
7	1	$\varepsilon_1=\varepsilon_2/4$	[+0.555] 9%	[+0.140] 9%	[+0.115] 13%	[+0.065] 13%
8	2	$\varepsilon_1=0$	[+0.595] 3%	0	[+0.115] 9%	[+0.040] 10%
7	0	$\varepsilon_1=-\varepsilon_2/4$	[+0.670] 15%	[–0.165] 15%	[+0.115] 9%	[+0.010] 23%
15	0	$\sigma_1=0$	[+0.670] 8%	[–0.220] 13%	[+0.115] 11%	0
15	1	$\varepsilon_1=-\varepsilon_2/2$	[+0.700] 10%	[–0.350] 10%	[+0.110] 10%	[–0.025] 15%
20	2	$\varepsilon_1=-\varepsilon_2$	[+0.740] 15%	[–0.740] 15%	[+0.085] 15%	[–0.095] 20%
15	2 2	$\sigma_2=0$	[+1.00] 22% [+1.00] 10%	[–2.05] 9% [–2.00] 10%	0	[–0.275] 8% [–0.270] 9%
8 15	1 0	$\varepsilon_2=-\varepsilon_1/2$	[+2.25] 6/% [+0.95] 8%	[–4.50] 6% [–1.90] 8%	[–0.125] 6% [0.000]	[–0.415] 5% [–0.265] 13%
7	2	$\varepsilon_2=-\varepsilon_1/4$	[+1.05] 18%	[–4.20] 18%	[–0.165] 24%	[–0.500] 11%
8	5	$\varepsilon_2=0$	0	[–4.10] 1%	[–0.275] 10%	[–0.555] 10%
7	1	$\varepsilon_2=\varepsilon_1/4$	[–0.95] 15%	[–3.80] 15%	[–0.390] 17%	[–0.590] 14%
8	3	$\varepsilon_2=\varepsilon_1/2$	[–1.75] 5%	[–3.50] 5%	[–0.455] 8%	[–0.560] 8%
7	3	$\varepsilon_2=\varepsilon_1$	[–2.80] 15%	[–2.80] 15%	[–0.505] 14%	[–0.505] 14%

3.4 Results for low crushing strength (3 times the fracture strength)

Results for low branch crushing strength set at only 3 (rather than 10) times higher than the corresponding fracture strength and subject to various types of loading, are listed in Table 3 and shown (with the same conventions as before) in Figure 5 for all-rod networks. The same is done for lightly reinforced random-aspect-ratio networks in Table 4 and Figure 6. Notice that the compressive stresses and strains listed and shown are much smaller than those for high branch crushing strength. In Figures 5(a) and 6(a), the Q3 part of the Kupfer-Gerstle envelope (Eq.1) corresponding to the strength in uniaxial compression is shown again as a black solid line and is matched very closely by the numerical results.

Almost all differences between the two sets of data are statistically insignificant. Furthermore, all failure envelopes appear convex, which is not the case for high crushing strength. Tension-dominated responses are

proven independent (to within statistical significance of the data) of branch aspect ratio (if physically plausible) and of nano-reinforcement (if "light"), again as expected. Furthermore, the reduction of branch crushing strength by 70% causes a reduction in the unidirectional compressive strength of networks by only 15–20%, a fact that reaffirms the predominance of transverse extension in the failure mechanism.

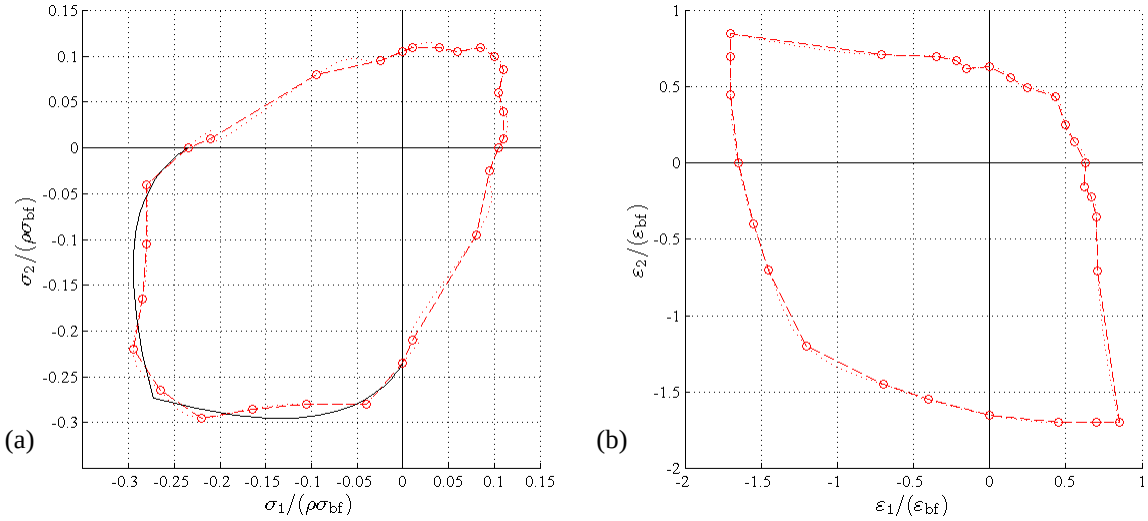

Figure 5: Failure envelopes for 15MHDx15MHD specimens of ***plain*** paste with branches of ***circular*** cross section and of crushing strength ***3 times*** the fracture strength in non-dimensionalized a) stress space and b) strain space. Both envelopes are traced by C^0 (dashed) and C^2 (dotted) splines. The Kupfer-Gerstle envelope is plotted as a black solid line.

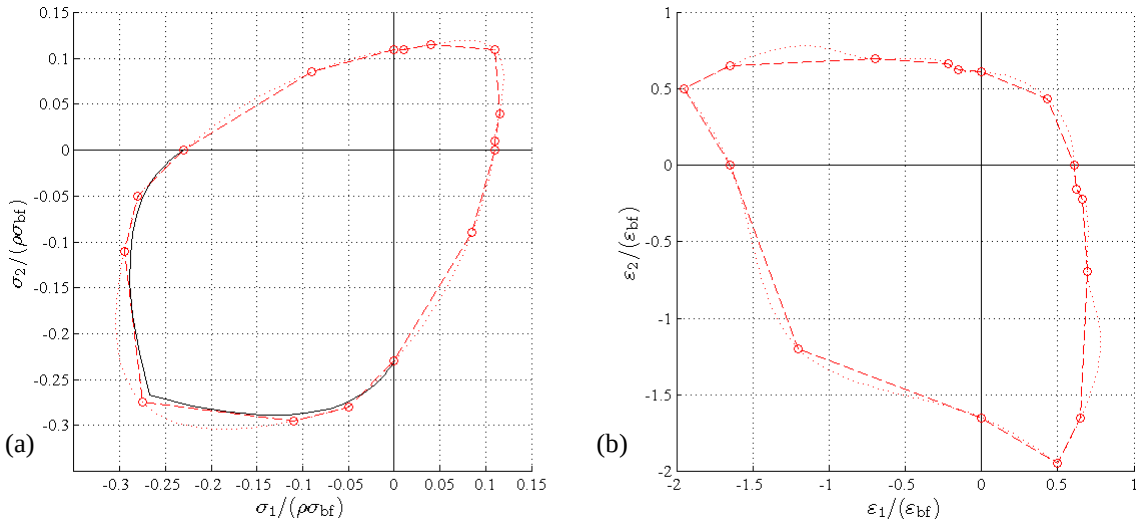

Figure 6: Failure envelopes for 15MHDx15MHD specimens of lightly(~0.1%) ***nano-reinforced*** paste with branches of ***elliptical*** cross section (random aspect ratio) and of ***c***rushing strength ***3 times*** the fracture strength in non-dimensionalized a) stress space and b) strain space. Envelopes are traced by C^0 (dashed) and C^2 (dotted) splines. The Kupfer-Gerstle envelope is plotted as a black solid line.

In uniaxial compression, there is noticeable difference in both stress and strain space between the point of limit stress (at lower strains) and the point of apparent incompressibility (at higher strains). The two points are not completely unrelated (in our earlier investigations of all-flake networks [10] they were found to differ by more than 30%), but they are not statistically identical either (they differ by less than 10% for all-rod networks and by about 15% for random-aspect-ratio networks).

The lowered crushing strength appears to render insignificant the effects of random aspect ratio of branch cross-sections on Q3 responses. The use of a random aspect ratio should clearly (if not dramatically) reduce Q3 strength; since no such trend is observed in the results, there must be a counterbalancing strengthening effect, due to the presence of light nano-reinforcement in the case where such is considered. Besides controlling material disintegration and maintaining higher post-peak stresses, light nano-reinforcement appears to move the attainment of peak stress to slightly lower strains and the occurrence of apparent incompressibility to slightly

higher strains (due to sustained confinement, to visualize this effect compare Tables 3 and 4). These last effects are not crisply visible, due to the high statistical variability of the results.

Table 3: Non-dimensional stress and strain data for 2D failure envelopes of 15MHD x 15MHD of ***plain*** paste specimens with branches of ***circular*** cross section and of crushing strength ***3 times*** the fracture strength.

N	n	Loading	$\varepsilon_2/\varepsilon_{bf}$	$\varepsilon_1/\varepsilon_{bf}$	$\sigma_2/(\rho\sigma_{bf})$	$\sigma_1/(\rho\sigma_{bf})$
8	1	$\varepsilon_1=\varepsilon_2$	[+0.435] 20%	[+0.435] 20%	[+0.100] 17%	[+0.100] 17%
8	2	$\varepsilon_1=\varepsilon_2/2$	[+0.495] 11%	[+0.255] 11%	[+0.110] 12%	[+0.085] 11%
8	3	$\varepsilon_1=\varepsilon_2/4$	[+0.560] 17%	[+0.140] 17%	[+0.105] 11%	[+0.060] 13%
8	1	$\varepsilon_1=0$	[+0.630] 6%	0	[+0.115] 7%	[+0.040] 10%
8	2	$\varepsilon_1=-\varepsilon_2/4$	[+0.620] 12%	[–0.155] 12%	[+0.110] 7%	[+0.010] 19%
8	1	$\sigma_1=0$	[+0.670] 11%	[–0.220] 16%	[+0.105] 9%	0
7	0	$\varepsilon_1=-\varepsilon_2/2$	[+0.700] 14%	[–0.350] 14%	[+0.095] 14%	[–0.025] 20%
8	1	$\varepsilon_1=-\varepsilon_2$	[+0.710] 12%	[–0.710] 12%	[+0.080] 13%	[–0.095] 13%
7	1 0	$\varepsilon_2=-\varepsilon_1/2$	[+0.85] 8% [+0.90] 7%	[–1.70] 8% [–1.80] 7%	[+0.010] 220% [0.000]	[–0.210] 14% [–0.195] 20%
8	4 5	$\sigma_2=0$	[+0.70] 20% [+0.90] 5%	[–1.70] 14% [–1.85] 5%	0	[–0.235] 7% [–0.215] 14%
8	3	$\varepsilon_2=-\varepsilon_1/4$	[+0.45] 9%	[–1.70] 9%	[–0.040] 33%	[–0.280] 17%
8	1	$\varepsilon_2=0$	0	[–1.65] 12%	[–0.105] 18%	[–0.280] 15%
8	2	$\varepsilon_2=\varepsilon_1/4$	[–0.40] 9%	[–1.55] 9%	[–0.165] 8%	[–0.285] 9%
8	3	$\varepsilon_2=\varepsilon_1/2$	[–0.70] 13%	[–1.45] 13%	[–0.220] 15%	[–0.295] 16%
8	0	$\varepsilon_2=\varepsilon_1$	[–1.20] 12%	[–1.20] 12%	[–0.265] 15%	[–0.265] 15%

Table 4: Non-dimensional stress and strain data for 2D failure envelopes of 15MHD x 15MHD of lightly (~0.1%) ***nano-reinforced*** paste specimens with branches of ***elliptical*** cross section (random aspect ratio) and of crushing strength ***3 times*** the fracture strength.

N	n	Loading	$\varepsilon_2/\varepsilon_{bf}$	$\varepsilon_1/\varepsilon_{bf}$	$\sigma_2/(\rho\sigma_{bf})$	$\sigma_1/(\rho\sigma_{bf})$
8	2	$\varepsilon_1=\varepsilon_2$	[+0.435] 14%	[+0.435] 14%	[+0.110] 12%	[+0.110] 12%
8	1	$\varepsilon_1=0$	[+0.610] 13%	0	[+0.115] 12%	[+0.040] 13%
8	1	$\varepsilon_1=-\varepsilon_2/4$	[+0.625] 14%	[–0.155] 14%	[+0.110] 12%	[+0.010] 29%
8	2	$\sigma_1=0$	[+0.665] 10%	[–0.220] 14%	[+0.110] 9%	0
8	1	$\varepsilon_1=-\varepsilon_2$	[+0.695] 10%	[–0.695] 10%	[+0.085] 12%	[–0.090] 12%
8	1 2	$\sigma_2=0$	[+0.65] 14% [+1.00] 10%	[–1.65] 8% [–2.00] 10%	0	[–0.230] 9% [–0.205] 12%
8	2	$\varepsilon_2=-\varepsilon_1/4$	[+0.50] 10%	[–1.95] 10%	[–0.050] 24%	[–0.280] 16%
8	2	$\varepsilon_2=0$	0	[–1.65] 4%	[–0.110] 12%	[–0.295] 8%
8	0	$\varepsilon_2=\varepsilon_1$	[–1.20] 9%	[–1.20] 9%	[–0.275] 12%	[–0.275] 12%

4 CONCLUSIONS

Failure envelopes for cementitious pastes are derived using a recently developed model of the material microstructure that uses a random lattice of hydrates growing out of a statistically uniform distribution of partially hydrated cement grains. Although the region modeled extends but a few micrometers in size, the mechanical behavior obtained under plane stress enforced through displacement control is thoroughly consistent with the experimentally derived failure envelopes for cement-like materials such as the Kupfer & Gerstle biaxial failure envelopes. Results are presented in the stress and strain space, enabling the observation and confirmation of familiar phenomena such as (a) the increased strength of the material under biaxial compression due to the confining action imparted by lateral restraint, (b) the increased resilience and fracture energy of cementitious materials reinforced with CNTs[14-17], (c) the effect of compression softening which refers to the reduction of compressive strength in the presence of transverse tensile strain. The most important aspect of these behavioral results is that they are obtained as calculated output of the analytical model, using as input a minimum number of material variables and no preconceived expressions as to the expected behavior; reproduced phenomena that characterize the behavior of cementitious materials include but are not limited to the apparent lateral dilation of compressed material beyond the peak, near incompressibility at the uniaxial compression limit point, a

reasonable ratio of compressive to tensile response, and the familiar characteristics of the biaxial failure envelope.

ACKNOWLEDGMENTS

This research has been co-financed by the European Union (European Social Fund – ESF) and Greek national funds through the Operational Program "Education and Lifelong Learning" of the National Strategic Reference Framework (NSRF) – Research Funding Program: "Thales – Democritus University of Thrace – Center for Multifunctional Nanocomposite Construction Materials" (MIS 379496). The third author also acknowledges the support of the University of Cyprus.

REFERENCES

[1] Powers, T.C. and Brownyard, T.L. (1946–1947), "Studies of the physical properties of hardened Portland cement paste", *ACI J. Proc.*, **43**:933–992.
[2] Feldman, R. F. and Sereda, P. J. (1968), "A model for hydrated Portland cement paste as deduced from sorption-length change and mechanical properties", *Materiaux et Construction*, **1**(6): 509–520.
[3] Reinhardt, H.W. (1985), "Fracture Mechanics of an Elastic Softening Material Like Concrete", HERON, Delft University of Technology, **29**(2).
[4] Qian, Z., Schlangen, E., Ye, G., and van Breugel, K. (2011), "3D Lattice Fracture Model: Theory and Computer Implementation", *Key Engineering Materials*, **452-453**:69–72.
[5] Constantinides, G. and Ulm, F.J.,(2007), "The nanogranular nature of C–S–H", *Journal of the Mechanics and Physics of Solids*, **55**:64–90.
[6] Cusatis, G., Pelessone, D., and Mencarelli, A. (2011) "Lattice Discrete Particle Model (LDPM) for Failure Behavior of Concrete. I: Theory". *Cement and Concrete Composites*, **33**(9):881–890.
[7] Etzold M., McDonald P., and Routh A., (2014), "Growth of sheets in 3D confinements – a model for the C–S–H meso structure", *Cement & Concrete Research*, **63**:137–142.
[8] Jennings H., (2008), "Refinements to colloid model of C-S-H in cement: CM-II", *Cement and Concrete Research*, **38**:275–289.
[9] Balopoulos V., Archontas, N., and Pantazopoulou, S. J. (2014), "Discrete Modelling and Simulation of Cementitious Materials Reinforced with Nanofibers", *CD-ROM Proceedings*, 3rd Int. RILEM Conf., SHCC3-TU Delft, Nov. 3-5, Dordrecht, Netherlands.
[10] Balopoulos, V., Archontas, N., and Pantazopoulou, S. J. (2015), "Discrete Model for the Structure and Strength of Cementitious Materials", under review, ASCE.
[11] Kupfer, H.&Gerstle, K. (1973), "Behaviour of Concrete under Biaxial Stress", *ASCE J. Eng. Mech. Div.*, **99**:852–866.
[12] Madureira, E. L.,Siqueira, T. M., and Rodrigues, E. C. (2013), "Creep strains on reinforced concrete columns", *Revista IBRACON de Estruturas e Materiais*, ISSN1983-4195, http://dx.doi.org/10.1590/S1983-41952013000400003
[13] Konsta-Gdoutos, M.S., Metaxa, Z.S. and Shah, S.P. (2010), "Highly Dispersed CNTs Reinforced Cement-Based Materials", *Cement & Concrete Res.*, **40**(7):1052–1059.
[14] Konsta-Gdoutos, M.S., Metaxa, Z.S. and Shah, S.P. (2010), "Multi-scale Mechanical and Fracture Characteristics and Early-age Strain Capacity of High Performance Carbon Nanotube/Cement Nanocomposites", *Cement and Concrete Composites*, **32**(2):110–115.
[15] Li G.Y., Wang P.M., Zhao X., (2005) "Mechanical behavior and microstructure of cement composites incorporating surface-treated MWCNTs", *Carbon* **43**:1239–1245.
[16] Metaxa, Z.S., Konsta-Gdoutos, M.S., and Shah, S.P. (2009), "CNT-Reinforced Concrete", *ACI SP* **276-2**:11–19.
[17] Tyson, B., Abu Al-Rub, R., Yazdanbakhsh, A., and Grasley, Z. (2011), "Carbon Nanotubes and Carbon Nanofibers for Enhancing the Mechanical Properties of Nanocomposite Cementitious Materials", *ASCE J. Materials in Civil Engineering*, **23**(7):1027–1035.
[18] Imran, I. and Pantazopoulou, S.J. (1996), "Experimental Study of Plain Concrete Under Triaxial Stress", *Materials Journal*, American Concrete Institute (ACI), **93**(6):589–601.